Research Highlights

A proposed picosatellite formation could provide volcanic plume height measurements.

Proof of concept tested using photographs taken from the International Space Station.

Astronaut photos of 2009 Sarychev eruption processed using structure-from-motion.

Plume height measured to a precision of ~200 m, also with ascent velocity estimates.

Results constrained a plume model to suggest a mass eruption rate of $2.6\times10^{6}$ kg $s^{-1}$.

Using picosatellites for 4-D imaging of volcanic clouds: proof of concept using ISS photography of the 2009 Sarychev Peak eruption

Klemen Zakšek[ab12*×], Mike R. James[c], Matthias Hort[b], Tiago Nogueira[a], Klaus Schilling[ad]

[a]Center for Telematics, Magdalene-Schoch-Str. 5, 97074 Würzburg, Germany; tiagon@telematik-zentrum.de (T.N.)

[b]University of Hamburg, Center for Earth System Research and Sustainability, Bundesstr. 55, D-20146, Hamburg, Germany; matthias.hort@uni-hamburg.de (M.H.)

[c]University of Lancaster, Lancaster Environment Centre, LA1 4YQ, Lancaster, United Kingdom; m.james@lancaster.ac.uk

[d]Julius-Maximilians-University Würzburg, Faculty of Mathematics and Computer Science, Am Hubland, 97074 Würzburg, Germany; schi@informatik.uni-wuerzburg.de

[1]Present address: ROSEN Group, Am Seitenkanal 8, 49811 Lingen, Germany

[2]Present address: University of Ljubljana, Faculty of Civil and Geodetic Engineering, Jamova 2, 1000 Ljubljana, Slovenia

[*]Corresponding author: klemen.zaksek@uni-hamburg.de

Abstract

Volcanic ash clouds can present an aviation hazard over distances of thousands of kilometres and, to help to mitigate this hazard, advanced numerical models are used to forecast ash dispersion in the atmosphere. However, forecast accuracy is usually limited by uncertainties in initial conditions such as the eruption rate and the vertical distribution of ash injected above the volcano. Here, we demonstrate the potential of the Telematics Earth Observation Mission (TOM) picosatellite formation, due for launch in 2020, to provide valuable information for constraining ash cloud dispersion models through simultaneous image acquisition from three satellites. TOM will carry commercial frame cameras. Using photogrammetric simulations, we show that such data should enable ash cloud heights to be determined with a precision (~30–140 m depending on configuration) comparable to the vertical resolution of lidar observations (30–180 m depending on the cloud height). To support these estimates, we processed photographs taken from the International Space Station of the 2009 Sarychev Peak eruption, as a proxy for TOM imagery. Structure-from-motion photogrammetric software successfully reconstructed the 3-D form of the ascending ash cloud, as well as surrounding cloud layers. Direct estimates of the precision of the ash cloud height measurements, as well as comparisons between independently processed image sets, indicate that a vertical measurement precision of ~200 m was achieved. Image sets acquired at different times captured the plume dynamics and enabled a mean ascent velocity of 14 m $s^{-1}$ to be estimated for regions above 7 km. In contrast, the uppermost regions of the column (at a measured cloud top height of ~11 km) were not ascending significantly, enabling us to constrain a 1-D plume ascent model, from which estimates for the vent size (50 m) and eruption mass flux ($2.6\times10^{6}$ kg $s^{-1}$) could be made. Thus, we demonstrate that nanosatellite imagery has the potential for substantially reducing uncertainties in ash dispersion models by providing valuable information on eruptive conditions.

Keywords

volcanic ash clouds, photogrammetry, cloud top height, Sarychev Peak, International Space Station, Telematics Earth Observation Mission, satellite formation, picosatellites

## 1 Introduction

Volcanic ash clouds represent a serious hazard to aviation and can cause widespread disruption. Numerical models are used to forecast ash cloud dispersion away from volcanoes. However, forecast accuracies are limited by poor constraints on eruption source parameters, including how high the ash is emplaced at the source, the mass eruption rate and the near-source plume dynamics (Bonadonna et al., 2012; Zehner, 2010). Uncertainties in these parameters can lead to particularly different forecast results in areas of high wind shear, e.g. Heinold et al. (2012), which can occur across height intervals of less than 500 m. Here, we show that pico- and nanosatellites can be used to provide valuable data to constrain ash cloud dispersion models by providing high quality estimates of ash cloud height and by constraining eruption models.

Ground-based measurements of ash cloud properties can be made by weather radar (Lacasse et al., 2004; Rose et al., 1995), specialised Doppler radar (Donnadieu, 2012; Hort and Scharff, 2016; Scharff et al., 2012) or lidar (Hervo et al., 2012; Mona et al., 2012). However, such observations are restricted by the spatial and temporal availability of instruments. Wider opportunities are provided by satellite remote sensing and a recent overview of satellite techniques for observations of volcanic Cloud Top Height (CTH) is given by Merucci et al. (2016). Operationally used height estimates are based on satellite observations of brightness temperature in $CO_2$ absorption bands (Frey et al., 1999), but these estimates are of low accuracy, e.g. with biases of >1 km and standard deviations of ~3 km (Holz et al., 2008). The most precise CTH measurements are achieved with satellite lidar such as the Cloud-Aerosol Lidar with Orthogonal Polarization (CALIOP) instrument on the CALIPSO satellite (NASA, 2014), with a horizontal resolution of 333–1667 m and vertical resolution of 30–180 m, depending on the distance to the ground. CALIOP has already been used successfully for volcanic ash cloud monitoring at Chaiten 2008 (Carn et al., 2009), Kasatochi 2008 (Karagulian et al., 2010), and Eyjafjallajökull 2010 (Stohl et al., 2011). However, by providing only nadir measurements over swath width of 1 km, the instrument has a revisit time of 16 days and so is unlikely to capture the earliest stages of eruptions, when estimation of initial eruption parameters is critical for timely and accurate ash dispersion modelling.

Future measurement opportunities will be offered by the continuously increasing capabilities of pico- and nanosatellites, e.g. CubeSats, with a mass between 1 and 10 kg, and a size approximately that of a toaster (Chin et al., 2008; Heidt et al., 2000; Puig-Suari et al., 2001; Schilling, 2006; Zurbuchen et al., 2016). Such platforms have many benefits over classic satellites including simpler and cheaper designs, faster build times and, consequently, many more units can be deployed. They can be applied to Earth surface monitoring (Selva and Krejci, 2012), and a constellation of >150 CubeSats from the company Planet is already delivering almost daily global coverage with up to 3 m spatial resolution in the visible spectrum (Planet, 2017). CubeSats are also currently being used for atmospheric monitoring, e.g. Stratos satellites for atmospheric profiles retrieval (Spire, 2017). Recent advances are developing the capability for in-orbit cooperation, to form self-organizing picosatellite formations (Schilling et al., 2017) rather than constellations (in which each satellite is individually controlled from ground). Formations will offer further interesting potential for innovative approaches in Earth observation applications and, here, we consider the forthcoming Telematics Earth Observation Mission (TOM), which is specifically designed for retrieving accurate CTH measurements by simultaneous acquisition of visible imagery from three different nanosatellites. The TOM is part of the Telematics International Mission (TIM; Schilling, 2017), and we focus on application of the TOM system for retrieving the height of volcanic ash clouds.

In this work, we first review photogrammetric approaches to volcanic CTH measurements, then quantify CTH measurement precision for TOM and assess its sensitivity through processing simulated photogrammetric image networks. Finally, to test the use of structure-from-motion photogrammetric software on images of a real plume, and to demonstrate what eruptive parameters can be derived, we provide a case study in which images of the Sarychev 2009 eruption captured by astronauts on the International Space Station (ISS), are processed and used to constrain a 1-D eruption model.

## 2 Ash cloud photogrammetry using satellite data

The earliest use of satellite data to estimate ash cloud heights with photogrammetric methods relied on measuring the length of the shadow cast by the cloud under known illumination conditions (Glaze et al., 1989; Prata and Grant, 2001; Simpson et al., 2000; Spinetti et al., 2013). However, more recent approaches, based on photogrammetric analysis of image pairs, use the observation of parallax shifts (apparent movement in the projection plane). Photogrammetric methods can have a substantial advantage over other techniques for measuring cloud top heights due to requiring fewer metadata and assumptions about atmospheric conditions (Merucci et al., 2016). However, clouds can move very rapidly (e.g. >50 m $s^{-1}$) and so, if images are not acquired simultaneously, additional estimates of cloud motion are also required (de Michele et al., 2016; Nelson et al., 2013; Urai, 2004). For a system to be fully independent of any additional atmospheric information, simultaneous observations of the same area must be available from two or more satellites (Zakšek et al., 2015).

### 2.1 Parallax observations from a single satellite

The most common approach to cloud photogrammetry is through instruments with multi-angle observation capabilities; for example, Prata and Turner (1997) used the forward and nadir views of the Along Track Scanning Radiometer (ATSR) to determine volcanic CTH for the 1996 Mt. Ruapehu eruption. ATSR was used also by Muller et al. (2007), who proposed that a combination of visible and thermal bands could yield information on multi-layer clouds. The Advanced Spaceborne Thermal Emission and Reflection Radiometer (ASTER) is also equipped with two cameras, and derived stereo cloud top heights have shown values that were ~1000 m higher than Moderate-resolution Imaging Spectroradiometer (MODIS) brightness temperature heights (Genkova et al., 2007). The Multi-angle Imaging SpectroRadiometer (MISR) has been utilized to retrieve volcanic CTH, optical depth, type, and shape of the finest particles for several eruptions (Flower and Kahn, 2017; Kahn and Limbacher, 2012; Nelson et al., 2013; Scollo et al., 2012, 2010; Stohl et al., 2011). The stereo infrared spectral imaging radiometer flown on mission STS-85 of the space shuttle in 1997 has also been used to estimate CTH (Lancaster et al., 2003). Comparing the results with coincident direct laser ranging measurements from the shuttle laser altimeter showed that the radiometer mean heights were about 100 m greater, although this could be reduced if the data are segmented first (Manizade et al., 2006).

The most recent volcanic CTH estimation used high resolution imagery from the Operational Land Imager (OLI) on Landsat 8 (de Michele et al., 2016), which retrieves multispectral channels at 30 m resolution and a panchromatic channel at 15 m resolution. Due to the very short time lag between the retrievals of different channels (less than 1 s), the baseline available to estimate CTH from a single satellite overpass (the distance between satellite positions at the time of retrieval for each spectral channel) is also relatively short (about 4 km from an orbit height of 705 km). Thus, a CTH accuracy better than ~500 m (de Michele et al., 2016) can only be achieved using high resolution imagery (~10 m) in which parallax can be resolved over such short baselines. If image resolution is coarser (e.g. 275 m for MISR), then a larger baseline is required.

### 2.2 Parallax observations from two different satellites

The use of two independent geostationary satellites for stereoscopic measurements of meteorological cloud-top heights was proposed several decades ago (Hasler, 1981; Hasler et al., 1991, 1983; Ondrejka and Conover, 1966; Wylie et al., 1998; Wylie and Menzel, 1989), with the results accurate to between 500 m (Hasler et al., 1983) and 1000 m (Seiz et al., 2007). For ash clouds, a combination of Meteosat-5/-8 TIR data has been used to monitor the eruption of Karthala in 2005 (Carboni et al., 2008) and Etna in 2013 (Merucci et al., 2016). A combination of satellites in low and geostationary orbits can also be used (Hasler et al., 1983) although this has only been applied so far to the 2010 Eyjafjallajökull (Zakšek et al.,

2013) and 2013 Etna eruptions (Corradini et al., 2016) with MODIS and Spinning Enhanced Visible and InfraRed Imager (SEVIRI) images.

## 2.3 Telematics Earth Observation Mission

The Telematics Earth Observation Mission (TOM) is a proposed satellite mission for photogrammetric observations of clouds (Zakšek et al., 2015) and will be realized as part of the international Telematics International Mission (TIM; Schilling, 2017), that is focussed on the application of picosatellites (CubeSats) for Earth observation purposes. TOM is dedicated to observing cloud top heights and will be launched as a formation of three satellites in 2020. The satellites will be operated as a single self-organising system capable of real-time reaction (Nogueira et al., 2017a, 2017b). In particular, autonomous cooperation between the spacecraft will allow synchronised imaging from multiple perspectives, to provide the basis for a novel remote cloud sensing approach, underpinned by least 30×20 km. This will allow unbiased CTH estimation also for clouds with several layers, which is important because wind direction and speed depend on the height. The satellites will be 3-axis stabilised and able to provide observations away from nadir with a pointing accuracy better than 1° (due to the use of an innovative miniature reaction wheel for efficient 3-axes-attitude control with a power demand <0.5 W). In addition, ground control points (GCPs) will be used to enable high quality image georeferencing.

The TOM project only started at the beginning of 2017 and the main mission characteristics are now defined (Schilling et al., 2017). TOM nanosatellites will be based on an underlying picosatellite bus, already demonstrated in earlier UWE (German abbreviation for Universität Würzburg Experimental-Satellit) missions (Busch et al., 2015; Schilling, 2006), but possibly enlarged to accommodate a commercial frame camera. The camera will not be radiometrically calibrated but, from an orbit of 600 km altitude, will give a spatial resolution in nadir of 10–40 m.

The most promising orbital arrangement for photogrammetric purposes uses three satellites (S1, S2 and S3) distributed over two different orbital planes. Satellites S1 and S3 (see Figure 1) fly in the same orbital plane, at an average separation of 170 km.  Satellite S2 is inserted in another orbital plane with a slight offset in right ascension of the ascending node, crossing the S1/S3 orbital plane (Figure 1), such that the maximum cross-track distance between S2 and the S1-S3 plane is approximately 50 km. Thus, S2 will be continuously changing its distance to both S1 and S3; the maximal distance will be 100 km and minimal 85 km (at such distances the communications link energy budget is still sufficient to enable inter-satellite contact). For a maximum slew angle of 30°, a single formation can provide at least one daylight observation window for a chosen area, per week. This three-satellite TOM is a proof of concept mission and, to deliver a higher overpass frequency for operational purposes, a constellation of TOM-similar formations would be required.

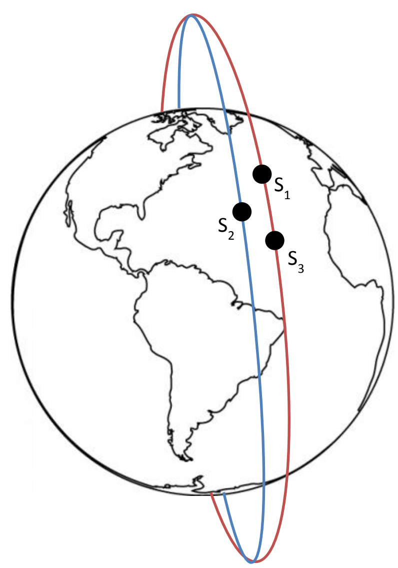


Figure 1. TOM formation.

# 3 Methods

## 3.1 CTH measurements from TOM: precision and sensitivities

To explore the potential precision of volcanic CTH measurements from photogrammetric analysis of TOM imagery, we constructed simulated image networks and processed them by bundle adjustment in the photogrammetric software VMS (Geometric Software, 2015). The ground and plume scene were represented by 5000 virtual 3-D points, distributed over a grid (with some random perturbations) to represent the position of surface features identified as tie points within images (Figure 2). The grid extended ±20 km from a central origin in *X* and *Y* on the ground (i.e. providing a tie point every ~570 m), and the ash cloud top was represented by elevating the points within a radius of 2 km of the origin (approximately 40 points) to a height of 10 km. The scene was observed by three identical virtual cameras (Table 1) positioned at locations suitable to represent TOM satellite locations, with their optic axes pointed at the origin so that the plume top was captured near the centre of the image. The pixel coordinates at which each 3-D point would appear in each image were then calculated, with small pseudo-random offsets applied from a normal distribution of prescribed standard deviation, $\sigma_i$, to represent image measurement precision. Simulations were carried out with three different values of $\sigma_i$, 0.5, 1 and 2 pixels, to represent a range of precision values typical of the type of feature detectors commonly used in structure-from-motion (SfM) software, under good to poor (i.e. weak image texture and image noise) imaging conditions. Atmospheric refraction was not simulated, but refraction effects are anticipated to be small for near-nadir viewing directions.

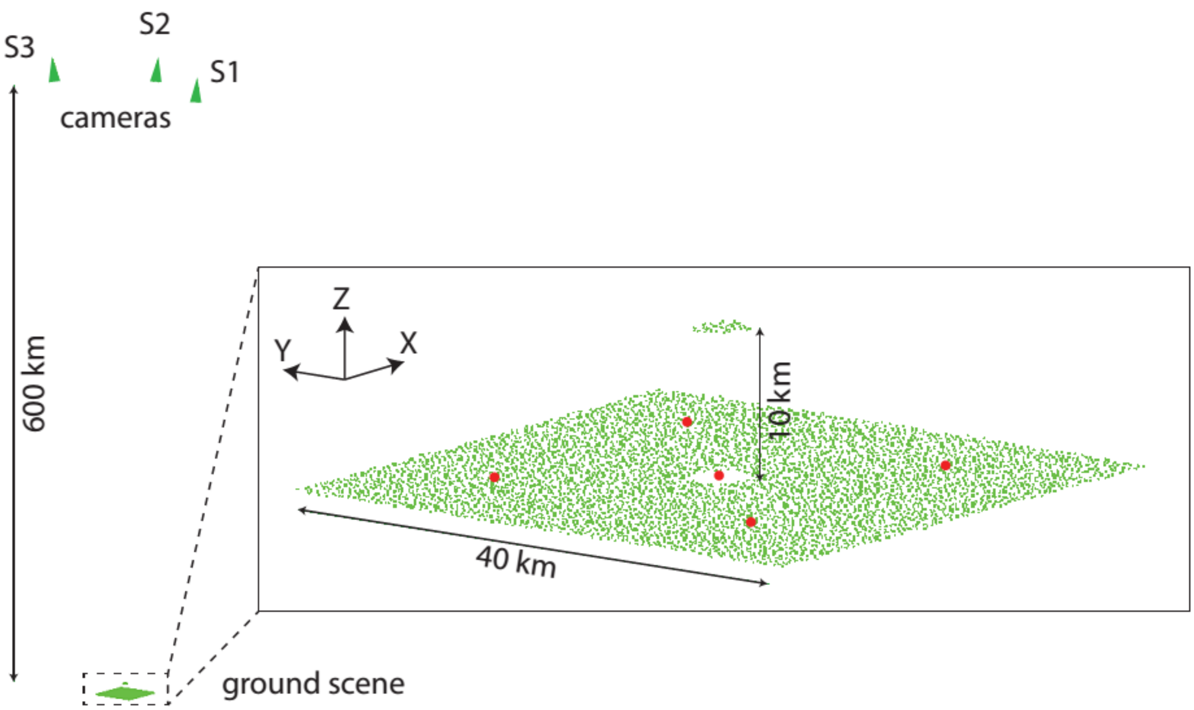


Figure 2. Simulated imaging scenario. The three TOM nanosatellites (triangles) are 600 km above the ground scene points. The enlarged inset shows the tie points representing the ground surface and the elevated tie points representing the top of the plume, located at 10 km above the origin. Larger (red) symbols represent GCP locations.

Table 1. Simulation parameter values.

| Parameter | Value |
|---|---|
| Cameras: | |
| Principal distance | 200 mm |
| Image size | 4000 × 3000 pixels |
| Pixel size | 3.3 µm |
| Survey geometry: | |
| Camera positions, [*X*, *Y*, *Z*] (km) | S1: [ 0  85 600]<br>S2: [50  0  600]<br>S3: [ 0 -85 600] |
| Nominal image footprint | ~40 × 30 km |
| Nominal ground sampling distance | ~10 m |

Photogrammetric control measurements were introduced through including the camera positions and orientations as known values, along with up to five virtual ground control points (GCPs). The precision of camera control data was defined as ±2 m for camera position and ±1° for camera orientation, reflecting the TOM specifications. GCPs were located in a 'dice' arrangement around the origin at maximum distances of ±10 km in *X* and *Y* (Figure 2). To assess the sensitivity of results to the precision of GCP measurements, simulations were carried out assuming different GCP precision values over the range of 5–100 m (in *X*, *Y* and *Z*). Bundle adjustments were processed using an invariant camera model, with the resulting VMS output providing coordinate precision estimates for each 3-D point. CTH measurement precision was then estimated by identifying the 3-D points that represented the plume top, and averaging their vertical precision values.

Bundle adjustments were also carried out without including control measurements, to assess the photogrammetric strength of the image networks alone (i.e. with the given imaging geometry and the defined image measurement precision, but independent of any georeferencing to an external coordinate system). Consequently, the resulting point coordinate precision estimates, given by adjustment under 'inner constraints' (Granshaw, 1980), can be considered to be the optimal values possible for the image network in isolation. Thus, comparing such results to equivalents obtained with control measurements gives insight into the relative contributions of photogrammetric and georeferencing aspects to the overall precision estimates. For example, in cases where georeferenced precision estimates are substantially weaker than those estimated by the inner constraints solution, then the precision-limiting factors are related to the georeferencing, and improving control (e.g. more, better distributed or more precisely surveyed GCPs) will have valuable effect.

## 3.2 Sarychev Peak eruption, imaging and analysis

To trial real space-based frame camera imagery for volcanic CTH measurements using the best data currently available as a proxy for TOM, we processed astronaut photographs of the eruption column from the 2009 Sarychev Peak eruption (Figure 3). The recent activity of Sarychev Peak, on Matua Island (Kuril islands, Russia) has been dominated by andesitic volcanism and, since about 500 AD, mainly by basaltic andesite (Martynov et al., 2015). For eruption modelling, Sarychev's Holocene activity has an average magma composition of $SiO_2$ 55 wt%, MgO 4 wt%, $TiO_2$ 0.8 wt%, $Al_2O_3$ 19 wt%, CaO 8 wt%, $Na_2O$ 3.5 wt%, $K_2O$ 1 wt%, and FeO 8 wt% (Martynov et al., 2015), but the volatile content, particularly for the 2009 eruption, is unknown. However, observations of strong condensation in the upper part of the eruption column (Figure 3) suggest a non-negligible amount of water was present in the melt prior to eruption. For the average magma composition above, the MELTS software (Asimow and Ghiorso, 1998; Ghiorso and Sack, 1995) yields an estimated liquidus temperature of about 1200 °C, for which the melt viscosity would be on the order of 500 Pa s with no water present (Giordano et al., 2008), but would significantly reduce with increasing water content.

During June 11–21, 2009, Sarychev Peak erupted explosively (Levin et al., 2010; Rybin et al., 2011), disrupting aviation traffic between the West coast of North America and East Asia. On June 12$^{th}$, the International Space Station (ISS) passed Sarychev Peak and astronauts photographed the eruption column (NASA, 2017). According to the official advisory of the Tokyo Volcanic Asch Advisory Centre, the ash reached a flight level 340, meaning that it might have reached a height of 10.4 km above the ground (Tokyo VAAC, 2009). No ground observations were available during the eruption. The images (Figure 3) reveal Matua Island through an opening in the clouds surrounding the vertically ascending column, which was topped by cap cloud (or pileus, seen in white in Figure 3), indicating rapid ascent and that the water content was high. On the right or lower right of each image, the volcanic ash is seen drifting away from the eruption column (Figure 3).

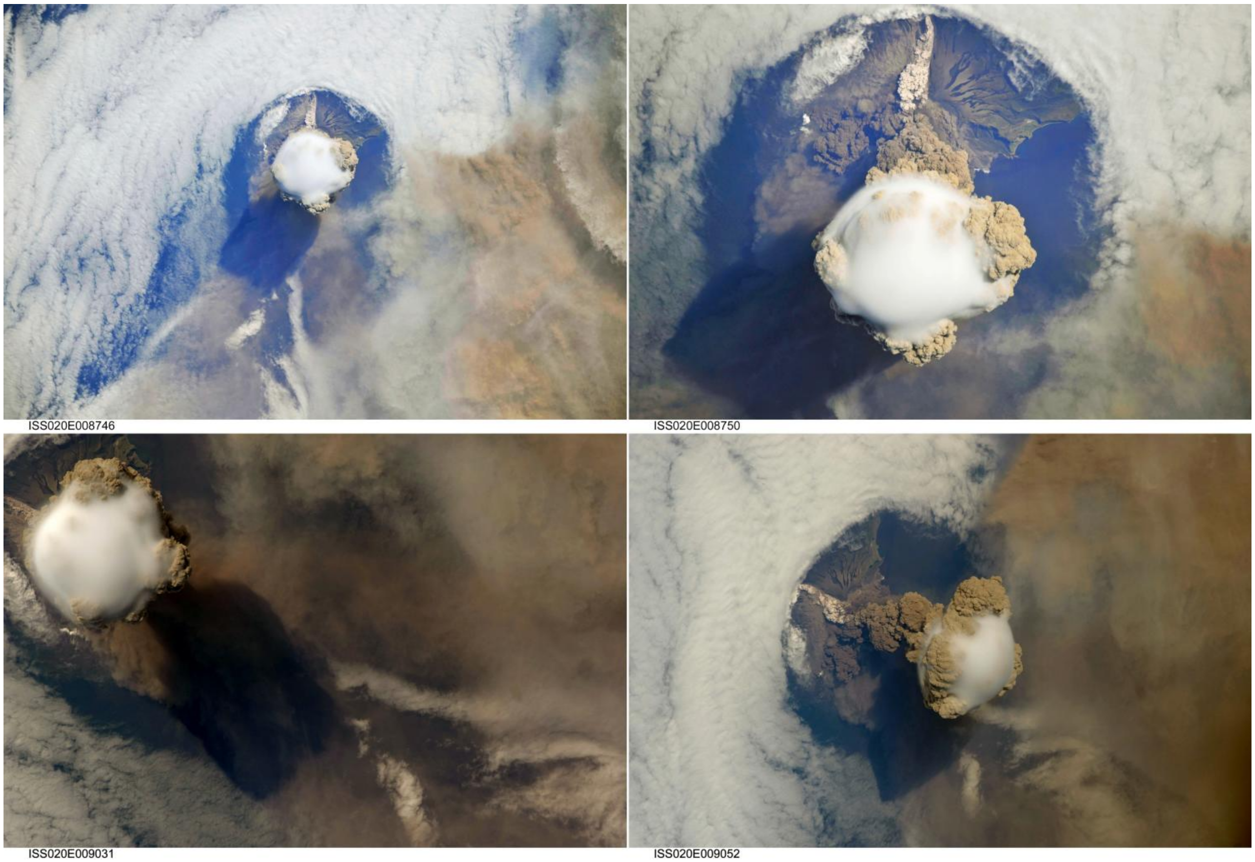


Figure 3. Example photos (ISS020E008746 taken with Nikon D3X camera and 300 mm lens, ISS020E008750 taken with Nikon D3X camera and 800 mm lens, ISS020E009031, and ISS020E009052 both taken with Nikon D2Xs camera and 400 mm lens) taken by ISS astronauts of the Sarychev Peak eruption on June 12$^{th}$ 2009 at approximately 22:16 UTC. Credit: Earth Science and Remote Sensing Unit, NASA Johnson Space Center (NASA, 2017).

During the astronaut observations, the eruption was recorded with three cameras from an ISS altitude of approximately 337 km (NASA, 2017):

- a Nikon D3X camera and 300 mm lens (5 images, over a 14 s long time-span),
- a Nikon D2Xs camera and 400 mm lens (31 images, over a 53 s long time-span), and

- a Nikon D3X camera and 800 mm lens (9 images, over a 27 s long time-span).

The images are not a perfect simulation-dataset for TOM because they were all acquired from the same platform (ISS), rather than simultaneously from different platforms. Thus, an appropriate baseline for photogrammetric analysis is only achieved by using images taken at different times, during which the eruption column is constantly evolving, and hence degrading photogrammetric analyses. However, ISS has an approximate speed of 7.7 km $s^{-1}$, which gives a suitable angular change with respect to a point on the Earth's surface of 6° in just 5 s, making a proof-of-concept photogrammetric analysis possible, in the absence of more appropriate data.

Structure-from-motion (SfM) processing was applied using PhotoScan Pro (v.1.2.6) software, with multiple selected image sets from each camera processed separately. Initial camera alignments were carried out using PhotoScan's 'high accuracy' setting. Due to the weak image network geometry (small numbers of images taken relatively close to each other, target far away), both GCPs and known camera positions had to be included as control measurements within the bundle adjustment in order to achieve useful results, and only focal length was adjusted within the camera model. Five natural features were identified in the imagery for GCPs, and their ground coordinates ascertained from Google Earth to an estimated relative precision of 20 m (in *X*, *Y* and *Z*). GCP positions in images were manually identified, then refined using a semi-automated patch matching algorithm (James et al., 2017a; James and Robson, 2012) although, in some cases, image noise prevented successful patch matching and manual values were retained.

Camera positions could be estimated by combining image time-stamps (provided in the images metadata) with the modelled ISS orbital path (Myflipside Media, 2007). For images acquired from the same camera in short succession, time-stamps have a relative precision of 0.01 s. The precision of the modelled orbit is ~100 m per coordinate (in a geocentric coordinate system based on the WGS 84 datum), and approximately the same error can be related to the errors in timing and 7.7 km $s^{-1}$ orbit speed of ISS. Considering the geographic position of the volcano and the vector of motion (predominantly West-East, meaning along Y axis), we estimated relative precisions for camera position control data of 150 m in *X* and *Z* direction and 250 m in the *Y* direction. Consequently, within the bundle adjustment, all control measurements (GCPs and camera positions) were defined with precision estimates, and PhotoScan's 'accuracy' settings for image measurements were adjusted appropriately to reflect the RMS image residuals on both GCPs and tie points (Table 2; James et al., 2017a).

However, because the cameras' internal clocks were not precisely synchronised to UTC (and could have drifted by ±10 s equivalent to ~80 km; personal communication with astronaut A. Gerst, European Space Agency), the absolute estimates of camera position were subject to much greater uncertainty along the orbital path. In order to determine the likely UTC timing offset value for any specified image set, repeated bundle adjustments were carried out to cover the range of camera positions representing an uncertainty of ±15 s in the absolute time-stamp values (tested at increments of 0.1 s). The most likely time offset was then determined by the minimum RMS (root mean square) misfit between the orbit-estimated camera control positions and those estimated by the bundle adjustment. Once an optimum time offset had been ascertained, the data were fully processed into a dense point cloud (using PhotoScan's 'medium' quality or point density setting), manually cleaned of outlier points and interpolated into a CTH map representing the highest points over a regular grid of 10" resolution (approximately 300 m).

The three different camera/lens combinations resulted in three independent collections of images, within each of which, different combinations of images were processed to assess the repeatability of results. The image combinations (Table 2) were selected to represent different mean times for the retrievals and different durations of observations (a long time span between images increased the viewing angle, but also increased uncertainty due to the evolution of the plume). As a further indicator of quality, coordinate precision estimates were also made for the 3-D points of individual photogrammetric models. However, in contrast to the VMS software used for the simulations (which outputs such precision estimates), PhotoScan does not provide point precision information directly, so a Monte Carlo approach was used; see James et al. (2017b) for details. The Monte Carlo method provides point coordinate precision estimates, but also gives additional insight into how much overall precision is limited by either photogrammetric considerations (which affect the relative shape of a model) or georeferencing considerations (which affect the location, orientation and scale of a model).

Table 2. Different scenarios for the sensitivity analyses. Bold rows indicate image sets used later as characteristic for the specific camera/lens combination.

| Scenario | [num. images] image IDs | Camera timing offset [s] | Corrected mean time of retrieval (UTC) | Duration of observation interval [s] | Viewing angle from ISS to volcano [°] | Number of points with CTH > 7 km | RMS discrepancy with control positions [m] | | RMS image residual magnitude [pixels] | |
|---|---|---|---|---|---|---|---|---|---|---|
| | | | | | | | Camera position | GCP | Tie points | GCP |
| D3X + 300 mm | | | | | | | | | | |
| I | [4] 8743–46 | -0.5 | 22:15:37.1 | 3.89 | 12.6 | 32 | 447 | 51 | 1.1 | 1.3 |
| **II** | **[4] 8743–46** | **-1.5** | **22:15:36.1** | **3.89** | **11.7** | **32** | **348** | **69** | **1.1** | **1.3** |
| III | [4] 8743–46 | -2.5 | 22:15:35.1 | 3.89 | 10.9 | 32 | 413 | 59 | 1.1 | 1.3 |
| D2Xs + 400 mm | | | | | | | | | | |
| **IV** | **[8] 9022–24; 9026–30** | **-6.3** | **22:15:25.0** | **5.70** | **8.4** | **438** | **234** | **73** | **1.5** | **1.6** |
| V | [4] 9035–38 | -7.0 | 22:15:35.6 | 4.99 | 11.3 | 420 | 265 | 61 | 1.3 | 1.0 |
| VI | [13] 9040–52 | -6.7 | 22:16:02.9 | 23.25 | 35.1 | 829 | 268 | 81 | 2.0 | 3.0 |
| D3X + 800 mm | | | | | | | | | | |
| VII | [8] 8738–42; 8747–49 | -2.5 | 22:15:35.1 | 20.19 | 10.9 | 1369 | 201 | 86 | 3.4 | 3.1 |
| **VIII** | **[5] 8738–42** | **-2.6** | **22:15:29.5** | **4.42** | **7.8** | **505** | **193** | **67** | **2.5** | **1.5** |
| IX | [3] 8747–49 | -2.7 | 22:15:44.1 | 3.58 | 19.1 | 868 | 77 | 102 | 2.6 | 1.7 |

# 4 Results

## 4.1 Simulated TOM CTH measurements: precision and sensitivities

The simulations demonstrated that, for TOM imaging geometry and GCP coordinates known to ~20 m or better, CTH precision was limited by image measurement precision and the number of GCPs used, and was insensitive to the precision of the GCP ground survey (Figure 4). Under these conditions, CTH precision scaled linearly with image measurement precision, $\sigma_i$; for example, with 5 GCPs, CTH precision increased from ~25 m for $\sigma_i$ = 0.5 pixel to ~100 m for $\sigma_i$ = 2 pixels. For a specific number of GCPs, the results can be generalised by curve fitting to the data (given in Figure 4 left panel) to give CTH precision estimates, $\sigma_{CTH}$, in metres to within 10% by the empirical equation

$$\sigma_{CTH} = a\sigma_i + b\sigma_{GCP}{}^{(c-d\sigma_i)} \qquad \text{Eq. 1.}$$

where *a*, *b*, *c* and *d* are derived constants ($\sigma_i$ is in pixels and $\sigma_{GCP}$ is in metres). For 5 GCPs (Figure 4, solid symbols), *a* = 50.4, *b* = 0.00761, *c* = 1.83 and *d* = 0.156.

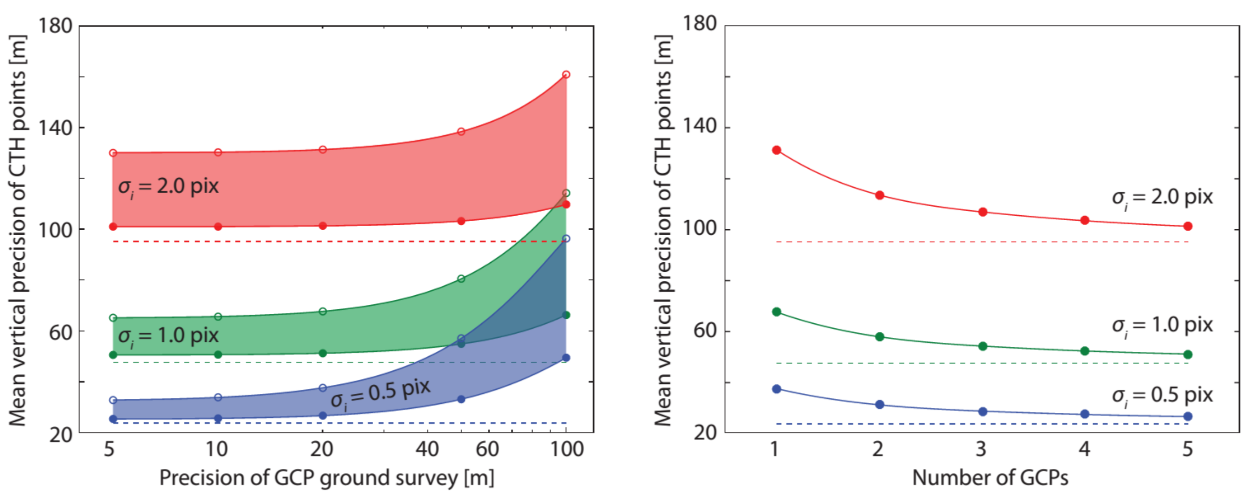


Figure 4. (Left panel) Estimated precision of CTH measurements from simulated image networks, for varying ground survey precision of GCPs. Results for three different image measurement precisions (with RMS image tie point residual, $\sigma_i$ = 0.5, 1 or 2 pixels) are shown, with the shaded areas enveloping

those obtained from networks incorporating 5 GCPs (solid symbols) and those with only 1 GCP (open symbols). (Right panel) Precision of CTH measurements estimated from the simulated image networks with varying numbers of GCPs. The different curves result from processing with three different image measurement precisions, $\sigma_i$ = 0.5, 1 or 2 pix, all processed using a ground survey precision of 20 m for the GCP(s). In both panels, the straight dashed lines illustrate the best possible precision from the photogrammetry alone (i.e. from an inner constraints solution), when precision is not diluted by weaknesses in the control and georeferencing.

As the number of GCPs is reduced from 5 to 1 GCP, CTH measurement precision degrades by ~30 % (Figure 4 right panel). Nevertheless, in conjunction with the camera position data, even using one GCP provides a reasonable scale constraint; if no GCPs are available and georeferencing relies on camera position and orientation data alone, CTH precision values degrade to 330, 660 and 1300 m for $\sigma_i$ = 0.5, 1 or 2 pix respectively.

### 4.2 Sarychev CTH measurements

The ISS image sets successfully enabled photogrammetric 3-D reconstructions of the ascending eruption column, dispersing ash plumes and a pyroclastic flow as well as cloud layers (selected 3-D point clouds are available as interactive visualisations online: D3X 300 mm – https://skfb.ly/6supW, D2Xs 400 mm – https://skfb.ly/6suLT and D3X 800 mm – https://skfb.ly/6su7B). Visual comparisons of the CTH maps derived from image sets from different cameras (Figure 5) show that they are broadly consistent in terms of the height and distribution of the observed layers. The top height of the eruption column reached >10 km and the condensation level for the pileus cloud was estimated at 7.5–8 km. Two plumes are drifting away from the vent region, with the higher one (at ~8 km altitude) dispersing to the South-East and the lower one (at ~3 km altitude) dispersing to the West. The dispersing plumes were particularly well observed with the Nikon D3X camera in combination with 300 mm lens (Figure 5, left panel), which provided a broader field of view than the other cameras.

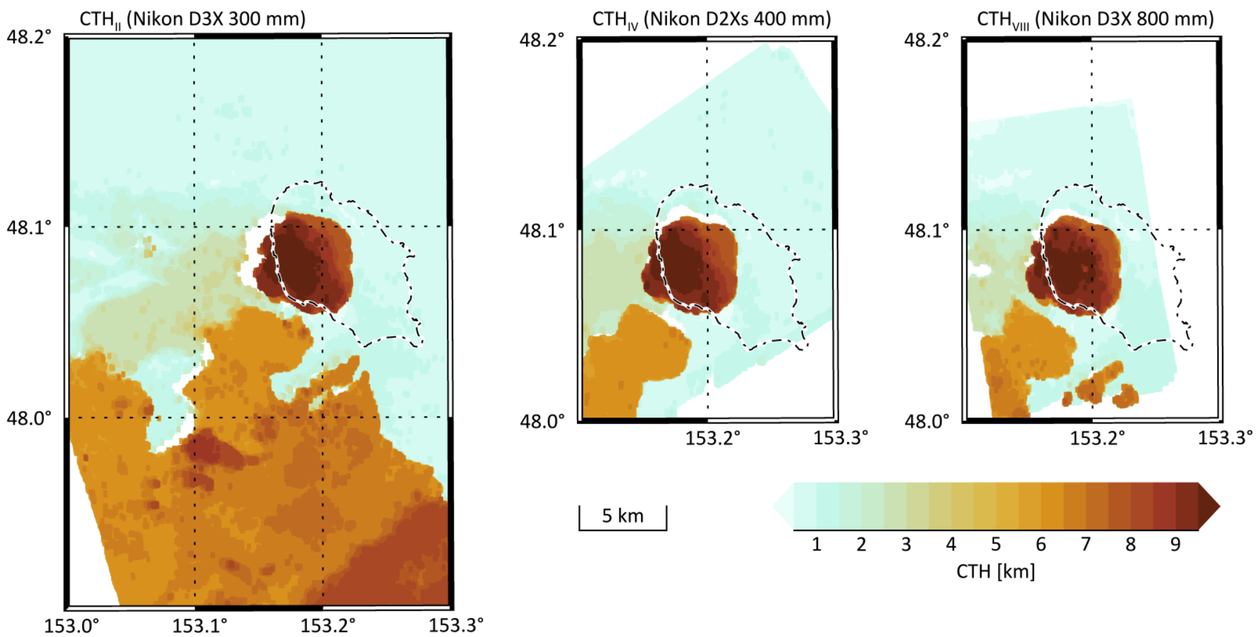


Figure 5. CTH over Matua Island (marked with a dash-dotted outline) estimated from the images taken with Nikon D3X camera with 300 mm lens (left, scenario II in Table 2), Nikon D2Xs camera with 400 mm lens (middle, scenario IV in Table 2), and Nikon D3X camera with 800 mm lens (right, scenario VIII in Table 2).

The next step of the analysis was to refine the control data by determining the timing offsets that represented the optimum camera positions, as indicated by minimum RMSE values on control (e.g. Figure 6). Note that the results (e.g. an RMSE of 348 m for the D3X camera with the 300 mm lens) reflect substantially greater uncertainty in camera position data than anticipated for TOM (~2 m), so the Sarychev case study was not expected to achieve the overall precisions demonstrated in the simulations.

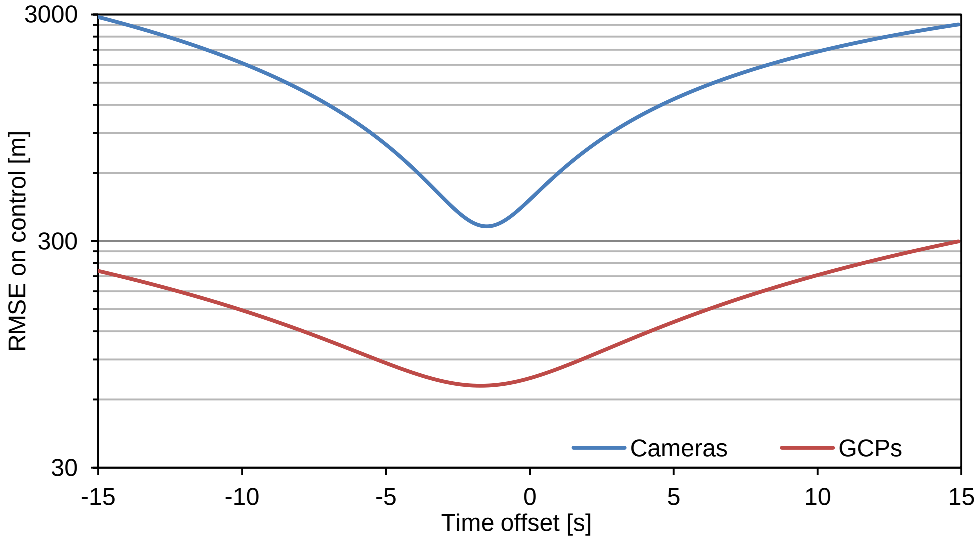


Figure 6. Optimization of the timing offset (and hence position) for the D3X camera with the 300 mm lens. A clear minimum is visible for a time offset of -1.5 s (RMSE on the camera positions is 348 m and 69.1 m on the GCPs). Note that the logarithmic scale on the *Y* axis.

For different combinations of input images from the same camera, the optimum timing offsets determined (for minimum RMSE values on either camera positions or on GCPs) differ by up to only ~0.2 s, giving confidence in the reproducibility of the CTH measurements. Nevertheless, to assess CTH sensitivity to uncertainty in timing, we calculated CTH differences for scenarios $CTH_{I-II}$ and $CTH_{III-II}$, in which conservative timing offset errors of ±1 s were introduced for the D3X camera with the 300 mm lens (representing systematic changes of almost 8 km in camera positions, Table 2). In areas close to the volcano, the resulting difference maps (Figure 7) only show substantial magnitude due to an apparent horizontal offset of the eruption column. With increasing distance from the volcano, vertical differences within the meteorological clouds in the North-East and in the ash cloud in the South-West become more pervasive and indicative of relative tilt between the different models. Both of these effects are in line with small model rotations about the GCPs, induced by the change in prescribed camera positions. However, with the GCPs located suitably close to the volcano (as here), the CTH estimates for the eruption column are shown to be relatively insensitive to limited systematic error in the camera positions.

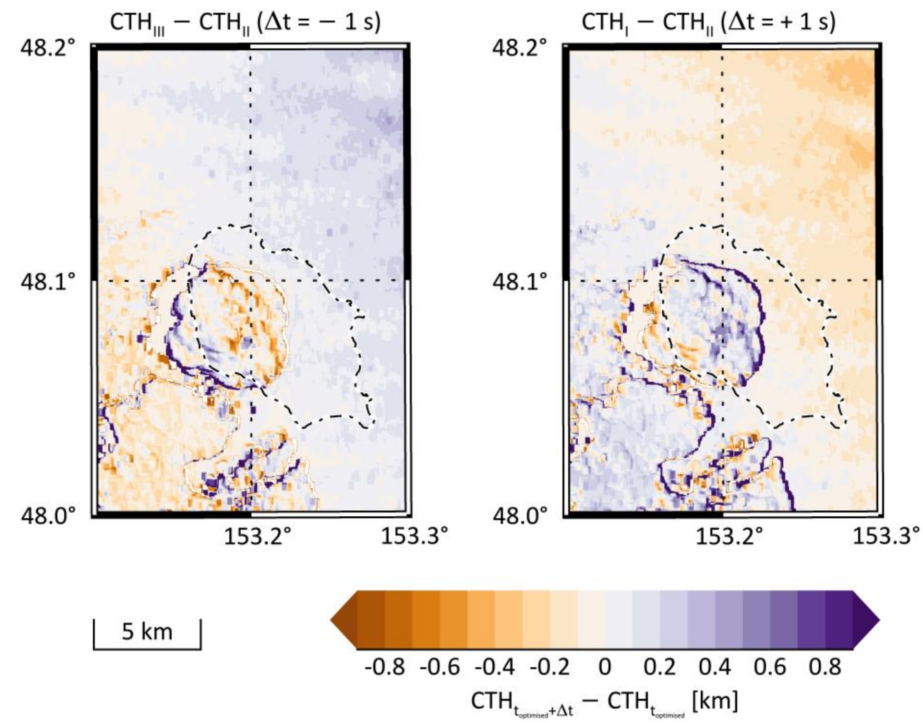


Figure 7. Comparison of CTH differences estimated from the images taken with Nikon D3X camera with 300 mm lens. Left panel: differences between scenarios I and II with a relative time offset -1 s. Right panel: differences between scenarios III and II with a relative time offset +1 s (Table 2).

Following optimization of the timing offsets, the CTH results from different scenarios (Table 2) should be almost consistent; nevertheless, given that the image timings are up to ~11 s apart, we might expect that some parts of the eruption column have evolved sufficiently to observe these differences in CTH maps. To carry out quantitative pairwise comparisons between the results from different cameras, we computed the determination coefficient ($r^2$) and the root mean square deviation (RMSD) for CTH map pairs from scenarios II, IV and VIII, over an area that contains data in all three maps (153.15°–153.23° E and 48.03°–48.11° N; Figure 5, Table 3). To remove the influence of outliers (which probably result mainly from horizontal variation at the edges of the eruption column), differences that exceeded 2 km were discarded. Although a few outliers <2 km still remain (Figure 8), they have only a small influence on the determination coefficient, which is ~0.99 in all three cases, and bias is insignificant (Table 3). Outlier influence on RMSD is more significant; if outliers >1 km were removed, RMSD values (Table 3) would be reduced to approximately 100 m. Thus, despite some noise, independent CTH values derived from the different cameras show excellent consilience. The small biases (Table 3) observed also in Figure 8 might be related to temporal evolution of the eruption column.

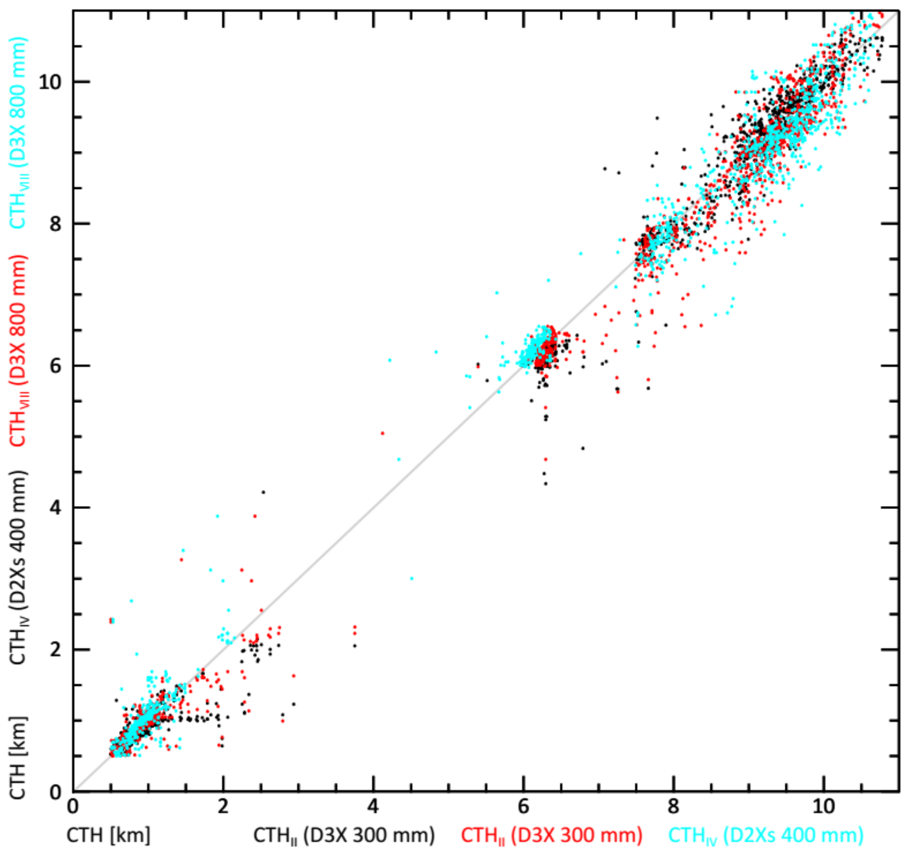


Figure 8. Comparisons of CTH values derived from different cameras for areas where all CTH maps contain data: D3X 300 mm vs. D2Xs 400 mm camera (black), D3X 300 mm vs. D3X 800 mm camera (red), and D2Xs 400 mm vs. D3X 800 mm camera (cyan). The grey line illustrates the 1:1 ratio.

Table 3. Comparison of CTH maps – basic statistics.

| | $r^2$ | RMSD [m] | Bias [m] |
|---|---|---|---|
| $CTH_{II}$ vs. $CTH_{IV}$ (D3x 300 mm vs. D2Xs 400 mm) | 0.992 | 327 | 45 |
| $CTH_{II}$ vs. $CTH_{VIII}$ (D3x 300 mm vs. D3X 800 mm) | 0.989 | 371 | 10 |
| $CTH_{IV}$ vs. $CTH_{VIII}$ (D2Xs 400 mm vs. D3X 800 mm) | 0.989 | 383 | 39 |

## 5 Discussion

Photogrammetric measurement of clouds is a very useful methodology for a range of different disciplines and, for example, could be also used for assessing anthropogenic aerosol, which has a substantial influence on climate and precipitation (Koren et al., 2004; Ramanathan et al., 2001; Rosenfeld, 2000). The photogrammetric approach used here is underpinned by assumptions of linear ray propagation and point reflection, so it is suitable for the dense near-vent portions of opaque volcanic ash clouds. We note, however, that in the case of a homogeneous background, also a semi-transparent cloud with optical depth (AOD) of 0.5 is already enough to run photogrammetric procedures (Merucci et al., 2016). Therefore, a satellite mission dedicated to cloud photogrammetry can also be considered as the first step towards 3D cloud tomography, which would enable volumetric data retrieval from dilute, dispersed plumes or cloud bodies (Levis et al., 2015).

Our results illustrate that with structure-from-motion photogrammetry and only a few space-based frame camera photographs, CTH measurements can be retrieved with a precision comparable to lidar vertical resolution. This demonstrates the great potential of photogrammetric methods and dedicated picosatellite missions like TOM for ash cloud monitoring. Formations of small satellites will offer significant measurement opportunities, in particular, as new miniature high precision 3-axes-control systems based on reaction wheels and high quality attitude determination sensors, become available. Our simulations show how CTH precision degrades systematically as the quality of control and image measurements is reduced (Figure 4), and that expected precisions can be modelled empirically to aid in mission planning and individual survey design.

The CTH measurements made for the Sarychev Peak case study did not reach the quality suggested by the TOM simulations. However, in contrast to TOM imagery, the astronaut photographs were subject to image measurement error due to an evolving plume and to unknown refraction effects resulting from the photographs being acquired through the spacecraft window. Nevertheless, CTH precision estimates for almost all scenarios were <250 m (Figure 9) and, although external validation is not directly possible (because thermal based CTH estimates have a larger uncertainty and the first lidar observations were only available from five days after the ISS observations (Prata et al., 2017)), our independently processed image sets demonstrate overall consistency (Figure 8). The most precise results were achieved by processing four images acquired over a duration of 5 s ($CTH_{V}$, D2Xs camera and 400 mm lens), giving a mean vertical precision for ash CTH measurements of ~170 m. Precision degraded to ~230 m with increasing duration of image capture (23 s for this camera, $CTH_{VI}$, Table 2), reflecting the greater magnitude of the image residuals. Thus, although increasing the number of images may be normally expected to improve photogrammetric precision, the opposite is observed due to the non-negligible evolution of the scene.

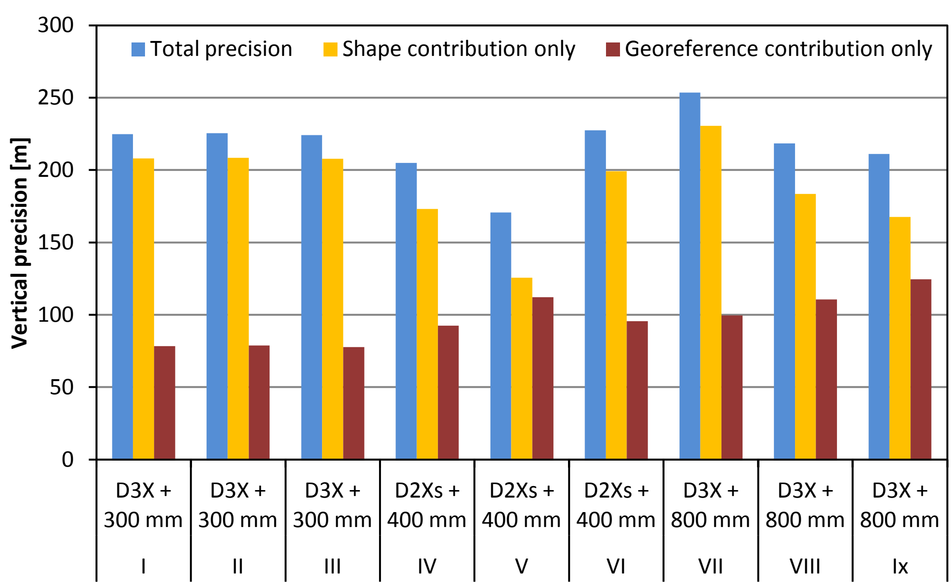

Figure 9. Vertical precision: total, considering only shape contribution, and considering only georeferenced contribution.

Our photogrammetric approach also makes it possible to consider the temporal evolution of the plume and to assess whether neutral buoyancy was reached. We then use a 1-D plume model to make rough estimates on eruption source parameters (vent radius, eruption exit velocity and mass eruption rate) that are important for plume dispersion modelling.

## 5.1 Temporal evolution of the eruption column

Through having processed image sets acquired at different times, we can assess the temporal evolution of the eruption column (Figure 10). We want to stress that we here focus the on upward movement, associated with some minor buoyancy-driven lateral expansion, but not substantial lateral advection of the plume due wind. Visual inspection of the photographs (Figure 3) shows a near-symmetric plume shape, which is dominated by vertical rather than horizontal motion. Therefore, we did not correct our results for the effect of wind. This can be, in a case of a clearly defined plume corrected as suggested by Nelson et al. (2013).

For each image set, mean CTH values were estimated for all pixels within the eruption column that were higher than 7, 8, 9 or 10 km. The evolution of these mean height values (Figure 10), demonstrates that the eruption column was still developing during the ISS overpass, with detectable ascent velocities when the lower parts of the column are included (a mean ascent velocity of ~14 m $s^{-1}$ for pixels ≥7 km high). Such velocities indicate that either 1) a part of the eruption column (a pulse) is rising or 2) the higher part of the eruption column is spreading. The highest parts of the column (≥10 km) show no significant upward velocity (0.9 m $s^{-1}$), suggesting that the neutral buoyancy height (NBH) had already been reached; the uppermost parts of the column will thus probably represent the region of overshoot.

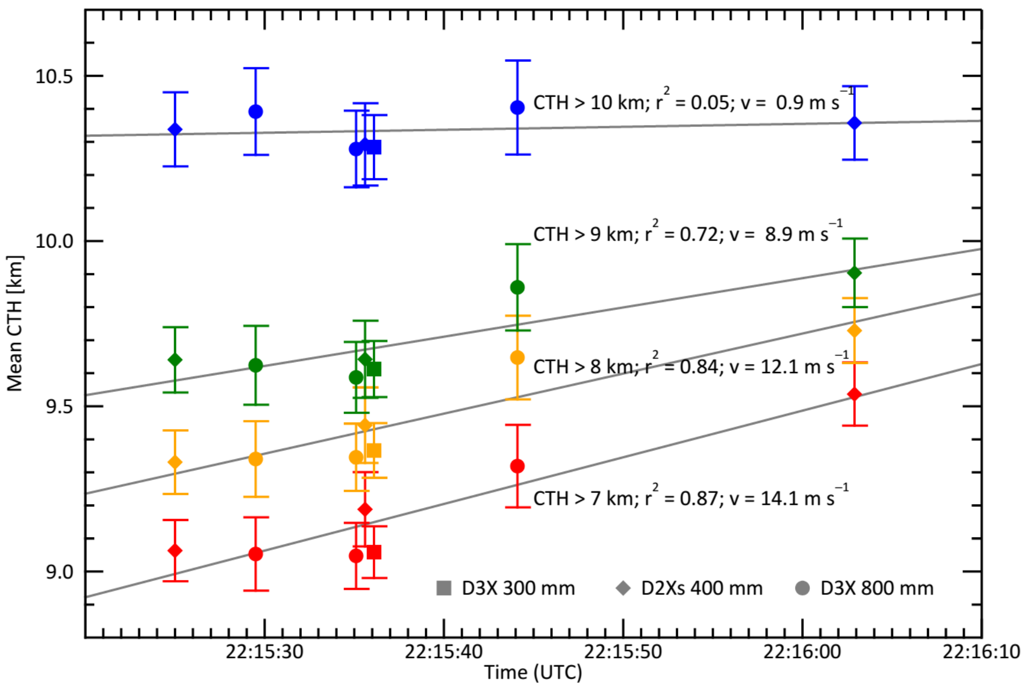


Figure 10. Comparison of mean CTH values estimated from combinations of images collected at different times (Table 2) for different height layers. The error bars represent the georeferencing component of the precision estimates, which will be systematic across the averaged CTH pixel values.

## 5.2 Eruption column modelling

Considering the maximum eruption column height of 10.6–11.1 km derived from the ISS observations, the mass flux at the vent can be estimated to be around $3\times10^{6}$ kg $s^{-1}$ using well established relationships between rise height of an eruption column and mass flux (Mastin, 2014). Given this approximate mass flux and the fact that there was no significant shearing of the eruption column due to wind (Figure 3), a straightforward 1-D model can be used to constrain estimates of initial water content, vent size and eruption velocity (Mastin, 2007). The results of the model calculations are compiled in Table 4.

Table 4. The results of the 1-D model calculations. The following parameters have been kept constant in all model calculations: atmospheric profile from Yuzhno-Sakhalinsk airport (46°53’N, 142°43’E,

http://weather.uwyo.edu/upperair/sounding.html) at 2009-06-13-00 UTC, vent elevation of 1500 m and eruption temperature of 1000 °C, which was chosen to reflect the fact that magma is not erupted at its liquidus temperature and that the erupted gas/ash mixture is typically over-pressurized upon eruption, leading to an initial cooling of the plume until it is equilibrated to ambient pressure. The atmospheric sounding data from Yuzhno-Sakhalinsk airport included relative humidity and entrained air adds additional water to the ascending plume. Note that changes in the eruption temperature (+/- 100 °C) would affect the height reported by less than 1%. The bold line indicates the most convincing combination of inputs and model estimates.

| Vent diameter [m] | Eruption velocity [m/s] | Water content [wt%] | Mass eruption rate [$10^6$ kg/s] | Onset of condensation [km] | NBH [km] | Column top height [km] |
|---|---|---|---|---|---|---|
| 50 | 80 | 3 | 0.73 | 5.0 | 9.2 | 10.7 |
| 50 | 80 | 2 | 1.00 | 5.8 | 9.4 | 11.0 |
| 50 | 80 | 1 | 2.10 | 6.7 | 9.6 | 11.8 |
| 50 | 100 | 3 | 0.92 | 5.8 | 9.4 | 10.9 |
| 50 | 100 | 2 | 1.40 | 6.0 | 9.5 | 11.3 |
| **50** | **100** | **1** | **2.60** | **7.0** | **9.8** | **12.1** |
| 50 | 120 | 3 | 1.10 | 5.5 | 9.4 | 11.1 |
| 50 | 120 | 2 | 1.60 | 6.1 | 9.6 | 11.5 |
| 50 | 120 | 1 | 3.20 | 7.2 | 9.8 | 12.4 |
| 50 | 140 | 3 | 1.30 | 5.6 | 9.5 | 11.2 |
| 50 | 140 | 2 | 1.90 | 6.3 | 9.6 | 11.7 |
| 50 | 140 | 1 | 3.70 | 7.4 | 9.9 | 12.6 |
| 75 | 60 | 3 | 1.20 | 5.8 | 9.5 | 11.3 |
| 75 | 60 | 2 | 1.80 | 6.5 | 9.6 | 11.7 |
| 75 | 60 | 1 | 3.60 | 7.7 | 10.0 | 12.8 |
| 75 | 80 | 3 | 1.70 | 6.1 | 9.6 | 11.6 |
| 75 | 80 | 2 | 2.50 | 6.8 | 9.8 | 12.1 |
| 75 | 80 | 1 | 4.70 | 8.0 | 10.0 | 13.2 |
| 40 | 100 | 3 | 0.59 | 4.8 | 8.9 | 10.5 |
| 40 | 100 | 2 | 0.87 | 5.6 | 9.3 | 10.8 |
| 40 | 100 | 1 | 1.70 | 6.4 | 9.6 | 11.5 |

The photogrammetric observations suggest a NBH of about 10 km (Figure 10), a maximum eruption column height of 10.6–11.1 km, and an estimated level of condensation of 7.5–8 km. We can now compare these observational data to the results of the model calculation. The modelled NBH is fairly constant in all calculations, but with a tendency to increase towards the observed value with increasing mass eruption rate and with decreasing water content. A low water content and high mass eruption rate scenario is also supported by the observation of the condensation level. This is somewhat contradicted by the observation of the CHT, that would call for lower mass eruption rates and higher water contents. The most convincing combination, which best matches model and photogrammetric estimates of condensation level and NBH, is a vent radius of ~50 m, an exit velocity of ~100 m $s^{-1}$, and an initial water content of 1 wt%, implying a mass eruption rate of $2.6 \times 10^6$ kg $s^{-1}$ during the ISS overpass (Table 4, bold line). This is also consistent with the NBH determined from the images, of around 10 km.

## 6 Conclusions

We have used images of the 2009 Sarychev Peak eruption taken by ISS astronauts to demonstrate that structure-from-motion photogrammetry with space-borne frame-camera imagery can produce robust estimates of volcanic CTH, which is one of the key source parameters for ash dispersion modelling. Our results have a vertical precision of ~200 m, which is comparable to lidar vertical resolution. However, our photogrammetric analysis also provides better spatial coverage and more detail of plume geometry than lidar, as well as offering the possibility of observing plume evolution over durations of order 1 min. Our results provide strong proof of concept in preparation for TOM, the picosatellite mission currently in development and dedicated to photogrammetric CTH observations through simultaneous image acquisition from multiple cooperating picosatellites. Simulated photogrammetric image networks for TOM suggest that vertical precisions of ~50 m could be achieved. By providing such data, TOM will offer wider possibilities, such as more accurate studies of multiple cloud layers and derivation of 3-D velocity vectors.

Acknowledgements:

This work is partially supported by the European Research Council (ERC) Advanced Grant 'NetSat' under the Grant Agreement No. 320377 and by the Bavarian Ministry of Economics for the Telematics Earth Observation Mission TOM. ISS images are courtesy of the Earth Science and Remote Sensing Unit, NASA Johnson Space Center and were obtained through the online Gateway to Astronaut Photography of Earth (http://eol.jsc.nasa.gov/). We would also like to thank Alexander Gerst for providing the background of photography on board ISS, Peter Webley for motivating this research with his wish of having better data for the Sarychev peak eruption, Stuart Robson for his ongoing provision and support of VMS software, and our colleagues Tristan Tzschichholz, Slavi Dombrovski, and Stephan Busch for valuable discussions.

References

Asimow, P.D., Ghiorso, M.S., 1998. Algorithmic modifications extending MELTS to calculate subsolidus phase relations. Am. Mineral. 83, 1127–1132. https://doi.org/10.2138/am-1998-9-1022

Bonadonna, C., Folch, A., Loughlin, S., Puempel, H., 2012. Future developments in modelling and monitoring of volcanic ash clouds: outcomes from the first IAVCEI-WMO workshop on Ash Dispersal Forecast and Civil Aviation. Bull. Volcanol. 74, 1–10. https://doi.org/10.1007/s00445-011-0508-6

Busch, S., Bangert, P., Dombrovski, S., Schilling, K., 2015. UWE-3, in-orbit performance and lessons learned of a modular and flexible satellite bus for future pico-satellite formations. Acta Astronaut. 117, 73–89. https://doi.org/10.1016/j.actaastro.2015.08.002

Carboni, E., Grainger, R., Thomas, G., Poulsen, C., Siddans, R., Smith, A., Sayer, A., Peters, D., 2008. Volcanic plume characterization using satellite measurements in the visible and thermal infrared. Presented at the USEReST 2008, Neaples, Italy.

Carn, S.A., Pallister, J.S., Lara, L., Ewert, J.W., Watt, S., Prata, A.J., Thomas, R.J., Villarosa, G., 2009. The Unexpected Awakening of Chaitén Volcano, Chile. Eos 90, 205–206. https://doi.org/200910.1029/2009EO240001

Chin, A., Coelho, R., Nugent, R., Munakata, R., Puig-Suari, J., 2008. CubeSat: The Pico-Satellite Standard for Research and Education, in: AIAA SPACE 2008 Conference & Exposition. Presented at the AIAA SPACE 2008 Conference & Exposition, AIAA SPACE Forum, American Institute of Aeronautics and Astronautics, San Diego, USA. https://doi.org/10.2514/6.2008-7734

Corradini, S., Montopoli, M., Guerrieri, L., Ricci, M., Scollo, S., Merucci, L., Marzano, F.S., Pugnaghi, S., Prestifilippo, M., Ventress, L.J., others, 2016. A multi-sensor approach for volcanic ash cloud retrieval and eruption characterization: The 23 November 2013 Etna lava fountain. Remote Sens. 8, 58.

de Michele, M., Raucoules, D., Arason, Þ., 2016. Volcanic Plume Elevation Model and its velocity derived from Landsat 8. Remote Sens. Environ. 176, 219–224. https://doi.org/10.1016/j.rse.2016.01.024

Donnadieu, F., 2012. Volcanological Applications of Doppler Radars: A Review and Examples from a Transportable Pulse Radar in L-Band, in: Bech, J. (Ed.), Doppler Radar Observations - Weather Radar, Wind Profiler, Ionospheric Radar, and Other Advanced Applications. InTech.

Fasano, G., Renga, A., D’Errico, M., 2014. Formation geometries for multistatic SAR tomography. Acta Astronaut. 96, 11–22. https://doi.org/10.1016/j.actaastro.2013.11.024

Flower, V.J.B., Kahn, R.A., 2017. Assessing the altitude and dispersion of volcanic plumes using MISR multi-angle imaging from space: Sixteen years of volcanic activity in the Kamchatka Peninsula, Russia. J. Volcanol. Geotherm. Res. 337, 1–15. https://doi.org/10.1016/j.jvolgeores.2017.03.010

Frey, R.A., Baum, B.A., Menzel, W.P., Ackerman, S.A., Moeller, C.C., Spinhirne, J.D., 1999. A comparison of cloud top heights computed from airborne lidar and MAS radiance data using CO2 slicing. J. Geophys. Res. Atmospheres 104, 24547–24555. https://doi.org/10.1029/1999JD900796

Genkova, I., Seiz, G., Zuidema, P., Zhao, G., Di Girolamo, L., 2007. Cloud top height comparisons from ASTER, MISR, and MODIS for trade wind cumuli. Remote Sens. Environ. 107, 211–222. https://doi.org/10.1016/j.rse.2006.07.021

Geometric Software, 2015. Vision Measurement System [WWW Document]. URL http://www.geomsoft.com/ (accessed 6.23.17).

Ghiorso, M.S., Sack, R.O., 1995. Chemical mass transfer in magmatic processes IV. A revised and internally consistent thermodynamic model for the interpolation and extrapolation of liquid-solid equilibria in magmatic systems at elevated temperatures and pressures. Contrib. Mineral. Petrol. 119, 197–212. https://doi.org/10.1007/BF00307281

Giordano, D., Russell, J.K., Dingwell, D.B., 2008. Viscosity of magmatic liquids: A model. Earth Planet. Sci. Lett. 271, 123–134. https://doi.org/10.1016/j.epsl.2008.03.038

Glaze, L.S., Francis, P.W., Self, S., Rothery, D.A., 1989. The 16 September 1986 eruption of Lascar volcano, north Chile: Satellite investigations. Bull. Volcanol. 51, 149–160. https://doi.org/10.1007/BF01067952

Granshaw, S.I., 1980. Bundle Adjustment Methods in Engineering Photogrammetry. Photogramm. Rec. 10, 181–207. https://doi.org/10.1111/j.1477-9730.1980.tb00020.x

Hasler, A.F., 1981. Stereographic Observations from Geosynchronous Satellites: An Important New Tool for the Atmospheric Sciences. Bull. Am. Meteorol. Soc. 62, 194–212. https://doi.org/10.1175/1520-0477(1981)062<0194:SOFGSA>2.0.CO;2

Hasler, A.F., Mack, R., Negri, A., 1983. Stereoscopic observations from meteorological satellites. Adv. Space Res. 2, 105–113. https://doi.org/10.1016/0273-1177(82)90130-2

Hasler, A.F., Strong, J., Woodward, R.H., Pierce, H., 1991. Automatic Analysis of Stereoscopic Satellite Image Pairs for Determination of Cloud-Top Height and Structure. J. Appl. Meteorol. 30, 257–281. https://doi.org/10.1175/1520-0450(1991)030<0257:AAOSSI>2.0.CO;2

Heidt, H., Puig-Suari, J., Moore, A., Nakasuka, S., Twiggs, R., 2000. CubeSat: A New Generation of Picosatellite for Education and Industry Low-Cost Space Experimentation. AIAAUSU Conf. Small Satell.

Heinold, B., Tegen, I., Wolke, R., Ansmann, A., Mattis, I., Minikin, A., Schumann, U., Weinzierl, B., 2012. Simulations of the 2010 Eyjafjallajökull volcanic ash dispersal over Europe using COSMO–MUSCAT. Atmos. Environ. 48, 195–204. https://doi.org/10.1016/j.atmosenv.2011.05.021

Hervo, M., Quennehen, B., Kristiansen, N.I., Boulon, J., Stohl, A., Fréville, P., Pichon, J.-M., Picard, D., Labazuy, P., Gouhier, M., Roger, J.-C., Colomb, A., Schwarzenboeck, A., Sellegri, K., 2012. Physical and optical properties of 2010 Eyjafjallajökull volcanic eruption aerosol: ground-based, Lidar and airborne measurements in France. Atmos Chem Phys 12, 1721–1736. https://doi.org/10.5194/acp-12-1721-2012

Holz, R.E., Ackerman, S.A., Nagle, F.W., Frey, R., Dutcher, S., Kuehn, R.E., Vaughan, M.A., Baum, B., 2008. Global Moderate Resolution Imaging Spectroradiometer (MODIS) cloud detection and height evaluation using CALIOP. J. Geophys. Res. Atmospheres 113, D00A19. https://doi.org/10.1029/2008JD009837

Hort, M., Scharff, L., 2016. Chapter 8 - Detection of Airborne Volcanic Ash Using Radar, in: Mackie, S., Cashman, K., Ricketts, H., Rust, A., Watson, M. (Eds.), Volcanic Ash. Elsevier, pp. 131–160. https://doi.org/10.1016/B978-0-08-100405-0.00013-6

James, M.R., Robson, S., 2012. Straightforward reconstruction of 3D surfaces and topography with a camera: Accuracy and geoscience application. J. Geophys. Res. Earth Surf. 117, F03017. https://doi.org/10.1029/2011JF002289

James, M.R., Robson, S., d'Oleire-Oltmanns, S., Niethammer, U., 2017a. Optimising UAV topographic surveys processed with structure-from-motion: Ground control quality, quantity and bundle adjustment. Geomorphology 280, 51–66. https://doi.org/10.1016/j.geomorph.2016.11.021

James, M.R., Robson, S., Smith, M.W., 2017b. 3-D uncertainty-based topographic change detection with structure-from-motion photogrammetry: precision maps for ground control and directly georeferenced surveys. Earth Surf. Process. Landf. 42, 1769–1788. https://doi.org/10.1002/esp.4125

Kahn, R.A., Limbacher, J., 2012. Eyjafjallajökull volcano plume particle-type characterization from space-based multi-angle imaging. Atmospheric Chem. Phys. Discuss. 12, 17943–17986. https://doi.org/10.5194/acpd-12-17943-2012

Karagulian, F., Clarisse, L., Clerbaux, C., Prata, A.J., Hurtmans, D., Coheur, P.F., 2010. Detection of volcanic SO2, ash, and H2SO4 using the Infrared Atmospheric Sounding Interferometer (IASI). J. Geophys. Res. Atmospheres 115, D00L02. https://doi.org/201010.1029/2009JD012786

Koren, I., Kaufman, Y.J., Remer, L.A., Martins, J.V., 2004. Measurement of the Effect of Amazon Smoke on Inhibition of Cloud Formation. Science 303, 1342–1345. https://doi.org/10.1126/science.1089424

Lacasse, C., Karlsdóttir, Larsen, G., Soosalu, H., Rose, W.I., Ernst, G.G.J., 2004. Weather radar observations of the Hekla 2000 eruption cloud, Iceland. Bull. Volcanol. 66, 457–473. https://doi.org/10.1007/s00445-003-0329-3

Lancaster, R.S., Spinhirne, J.D., Manizade, K.F., 2003. Combined Infrared Stereo and Laser Ranging Cloud Measurements from Shuttle Mission STS-85. J. Atmospheric Ocean. Technol. 20, 67–78. https://doi.org/10.1175/1520-0426(2003)020<0067:CISALR>2.0.CO;2

Levin, B.W., Rybin, A.V., Vasilenko, N.F., Prytkov, A.S., Chibisova, M.V., Kogan, M.G., Steblov, G.M., Frolov, D.I., 2010. Monitoring of the eruption of the Sarychev Peak Volcano in Matua Island in

2009 (central Kurile islands). Dokl. Earth Sci. 435, 1507–1510. https://doi.org/10.1134/S1028334X10110218

Levis, A., Schechner, Y.Y., Aides, A., Davis, A.B., 2015. Airborne Three-Dimensional Cloud Tomography. Presented at the Proceedings of the IEEE International Conference on Computer Vision, pp. 3379–3387.

Manizade, K.F., Spinhirne, J.D., Lancaster, R.S., 2006. Stereo Cloud Heights From Multispectral IR Imagery via Region-of-Interest Segmentation. IEEE Trans. Geosci. Remote Sens. 44, 2481–2491. https://doi.org/10.1109/TGRS.2006.873339

Martynov, Y.A., Rybin, A.V., Degterev, A.V., Ostapenko, D.S., Martynov, A.Y., 2015. Geochemical evolution of volcanism of Matua Island in the Central Kurils. Russ. J. Pac. Geol. 9, 11–21. https://doi.org/10.1134/S1819714015010042

Mastin, L.G., 2014. Testing the accuracy of a 1-D volcanic plume model in estimating mass eruption rate. J. Geophys. Res. Atmospheres 119, 2013JD020604. https://doi.org/10.1002/2013JD020604

Mastin, L.G., 2007. A user-friendly one-dimensional model for wet volcanic plumes. Geochem. Geophys. Geosystems 8, Q03014. https://doi.org/10.1029/2006GC001455

Merucci, L., Zakšek, K., Carboni, E., Corradini, S., 2016. Stereoscopic Estimation of Volcanic Ash Cloud-Top Height from Two Geostationary Satellites. Remote Sens. 8, 206. https://doi.org/10.3390/rs8030206

Mona, L., Amodeo, A., D'Amico, G., Giunta, A., Madonna, F., Pappalardo, G., 2012. Multi-wavelength Raman lidar observations of the Eyjafjallajökull volcanic cloud over Potenza, southern Italy. Atmos Chem Phys 12, 2229–2244. https://doi.org/10.5194/acp-12-2229-2012

Muller, J.-P., Denis, M.-A., Dundas, R.D., Mitchell, K.L., Naud, C., Mannstein, H., 2007. Stereo cloud-top heights and cloud fraction retrieval from ATSR-2. Int. J. Remote Sens. 28, 1921. https://doi.org/10.1080/01431160601030975

Myflipside Media, 2007. ISSTracker ~ Space Station Historical Locations [WWW Document]. URL http://www.isstracker.com/historical (accessed 6.25.17).

NASA, 2017. Gateway to Astronaut Photography of Earth [WWW Document]. URL https://eol.jsc.nasa.gov/ (accessed 4.22.17).

NASA, 2014. CALIPSO - Cloud-Aerosol Lidar and Infrared Pathfinder Satellite Observations [WWW Document]. URL http://www-calipso.larc.nasa.gov/ (accessed 1.11.14).

Nelson, D.L., Garay, M.J., Kahn, R.A., Dunst, B.A., 2013. Stereoscopic Height and Wind Retrievals for Aerosol Plumes with the MISR INteractive eXplorer (MINX). Remote Sens. 5, 4593–4628. https://doi.org/10.3390/rs5094593

Nogueira, T., Fratini, S., Schilling, K., 2017a. Planning and Execution to Support Goal-based Operations for NetSat: a Study, in: Proceedings of the 10th International Workshop on Planning and Scheduling for Space. Presented at the IWPSS 2017, Pittsburgh.

Nogueira, T., Fratini, S., Schilling, K., 2017b. Autonomously controlling flexible timelines: From domain-independent planning to robust execution, in: 2017 IEEE Aerospace Conference. Presented at the 2017 IEEE Aerospace Conference, pp. 1–15. https://doi.org/10.1109/AERO.2017.7943603

Ondrejka, R.J., Conover, J.H., 1966. Note on the stereo interpretation of nimbus ii apt photography. Mon. Weather Rev. 94, 611–614. https://doi.org/10.1175/1520-0493(1966)094<0611:NOTSIO>2.3.CO;2

Planet, 2017. Planet Monitoring [WWW Document]. Planet. URL https://www.planet.com/products/monitoring/ (accessed 7.19.17).

Prata, A.J., Grant, I.F., 2001. Retrieval of microphysical and morphological properties of volcanic ash plumes from satellite data: Application to Mt Ruapehu, New Zealand. Q. J. R. Meteorol. Soc. 127, 2153–2179. https://doi.org/10.1002/qj.49712757615

Prata, A.J., Turner, P.J., 1997. Cloud-top height determination using ATSR data. Remote Sens. Environ. 59, 1–13. https://doi.org/10.1016/S0034-4257(96)00071-5

Prata, A.T., Young, S.A., Siems, S.T., Manton, M.J., 2017. Lidar ratios of stratospheric volcanic ash and sulfate aerosols retrieved from CALIOP measurements. Atmos Chem Phys 17, 8599–8618. https://doi.org/10.5194/acp-17-8599-2017

Puig-Suari, J., Turner, C., Twiggs, R., 2001. CubeSat: The Development and Launch Support Infrastructure for Eighteen Different Satellite Customers on One Launch. AIAAUSU Conf. Small Satell.

Ramanathan, V., Crutzen, P.J., Kiehl, J.T., Rosenfeld, D., 2001. Aerosols, Climate, and the Hydrological Cycle. Science 294, 2119–2124. https://doi.org/10.1126/science.1064034

Rose, W.I., Kostinski, A.B., Kelley, L., 1995. Real time C band radar observations of 1992 eruption clouds from Crater Peak/Spurr Volcano, Alaska. U Geol. Surv. Bull. 2139, 19–26.

Rosenfeld, D., 2000. Suppression of Rain and Snow by Urban and Industrial Air Pollution. Science 287, 1793–1796. https://doi.org/10.1126/science.287.5459.1793

Rybin, A., Chibisova, M., Webley, P., Steensen, T., Izbekov, P., Neal, C., Realmuto, V., 2011. Satellite and ground observations of the June 2009 eruption of Sarychev Peak volcano, Matua Island, Central Kuriles. Bull. Volcanol. 73, 1377–1392. https://doi.org/10.1007/s00445-011-0481-0

Scharff, L., Ziemen, F., Hort, M., Gerst, A., Johnson, J.B., 2012. A detailed view into the eruption clouds of Santiaguito volcano, Guatemala, using Doppler radar. J. Geophys. Res. Solid Earth 117, B04201. https://doi.org/10.1029/2011JB008542

Schilling, K., 2006. Design of pico-satellites for education in systems engineering. IEEE Aerosp. Electron. Syst. Mag. 21, S_9-S_14. https://doi.org/10.1109/MAES.2006.1684269

Schilling, K., Tzschichholz, T., Loureiro, G., Zhang, Y., Steyn, W.H., Beltrame, G., De Lafontaine, J., Schlacher, K., 2017. Paper information (36789) — IAF, in: GLEX 2017 Proceedings. Presented at the Global Space Exploration Conference (GLEX 2017 ), IAF, Beijing, China, p. GLEX-1 7-12.1.4x36789.

Scollo, S., Folch, A., Coltelli, M., Realmuto, V.J., 2010. Three-dimensional volcanic aerosol dispersal: A comparison between Multiangle Imaging Spectroradiometer (MISR) data and numerical simulations. J. Geophys. Res. 115, D24210. https://doi.org/201010.1029/2009JD013162

Scollo, S., Kahn, R.A., Nelson, D.L., Coltelli, M., Diner, D.J., Garay, M.J., Realmuto, V.J., 2012. MISR observations of Etna volcanic plumes. J. Geophys. Res. 117, D06210. https://doi.org/10.1029/2011JD016625

Seiz, G., Tjemkes, S., Watts, P., 2007. Multiview Cloud-Top Height and Wind Retrieval with Photogrammetric Methods: Application to Meteosat-8 HRV Observations. J. Appl. Meteorol. Climatol. 46, 1182–1195. https://doi.org/10.1175/JAM2532.1

Selva, D., Krejci, D., 2012. A survey and assessment of the capabilities of Cubesats for Earth observation. Acta Astronaut. 74, 50–68. https://doi.org/10.1016/j.actaastro.2011.12.014

Simpson, J.J., McIntire, T., Jin, Z., Stitt, J.R., 2000. Improved Cloud Top Height Retrieval under Arbitrary Viewing and Illumination Conditions Using AVHRR Data. Remote Sens. Environ. 72, 95–110. https://doi.org/10.1016/S0034-4257(99)00095-4

Spinetti, C., Barsotti, S., Neri, A., Buongiorno, M.F., Doumaz, F., Nannipieri, L., 2013. Investigation of the complex dynamics and structure of the 2010 Eyjafjallajökull volcanic ash cloud using multispectral images and numerical simulations. J. Geophys. Res. Atmospheres 118, 4729–4747. https://doi.org/10.1002/jgrd.50328

Spire, 2017. Rapidly Refreshed Satellite Based Data [WWW Document]. https://spire.com/. URL https://spire.com/ (accessed 7.19.17).

Stohl, A., Prata, A.J., Eckhardt, S., Clarisse, L., Durant, A., Henne, S., Kristiansen, N.I., Minikin, A., Schumann, U., Seibert, P., Stebel, K., Thomas, H.E., Thorsteinsson, T., Tørseth, K., Weinzierl, B.,

2011. Determination of time- and height-resolved volcanic ash emissions for quantitative ash dispersion modeling: the 2010 Eyjafjallajökull eruption. Atmospheric Chem. Phys. 11, 5541–5588. https://doi.org/10.5194/acpd-11-5541-2011

Tokyo VAAC, 2009. Volcanic Ash Advisory, 00:00 UTC 13 Jun 2009, Sarychev Peak. Tokyo VAAC, Tokyo, Japan.

Urai, M., 2004. Sulfur dioxide flux estimation from volcanoes using Advanced Spaceborne Thermal Emission and Reflection Radiometer—a case study of Miyakejima volcano, Japan. J. Volcanol. Geotherm. Res. 134, 1–13. https://doi.org/10.1016/j.jvolgeores.2003.11.008

Wylie, D.P., Menzel, W.P., 1989. Two Years of Cloud Cover Statistics Using VAS. J. Clim. 2, 380–392. https://doi.org/10.1175/1520-0442(1989)002<0380:TYOCCS>2.0.CO;2

Wylie, D.P., Santek, D., Starr, D.O., 1998. Cloud-Top Heights from GOES-8 and GOES-9 Stereoscopic Imagery. J. Appl. Meteorol. 37, 405–413. https://doi.org/10.1175/1520-0450(1998)037<0405:CTHFGA>2.0.CO;2

Zakšek, K., Hort, M., Zaletelj, J., Langmann, B., 2013. Monitoring volcanic ash cloud top height through simultaneous retrieval of optical data from polar orbiting and geostationary satellites. Atmospheric Chem. Phys. 13, 2589–2606.

Zakšek, K., Valdatta, M., Oštir, K., Hort, M., Marsetič, A., Bellini, N., Rastelli, D., Locarini, A., Naldi, S., 2015. Clouds Height Mission, in: Sandau, R., Kawashima, R., Nakasuka, S., Sellers, J.J. (Eds.), Inventive Ideas for Micro/Nano-Satellites The MIC3 Report, IAA Book Series. International Academy of Astronautics, Paris (France).

Zehner, C., 2010. Monitoring volcanic ash from space, in: Monitoring Volcanic Ash from Space. Presented at the ESA-EUMETSAT workshop on the 14 April to 23 May 2010 eruption at the Eyjafjöjull volcano, South Iceland, Frascati, Italy. https://doi.org/10.5270/atmch-10-01

Zurbuchen, H.T., von Steiger, R., Bartalev, S., Dong, X., Falanga, M., Fléron, R., Gregorio, A., S. Horbury, T., Klumpar, D., Küppers, M., Macdonald, M., Millan, R., Petrukovich, A., Schilling, K., Wu, J., Yan, J., 2016. Performing High-Quality Science on CubeSats. Space Res. Today 196, 11–30. https://doi.org/10.1016/j.srt.2016.07.011